Applied Physics Letters

Nondestructive inspection of metallic microstructure chips based on photoacoustic remote sensing microscopy

Cite as: Appl. Phys. Lett. **120**, 182201 (2022); https://doi.org/10.1063/5.0090897
Submitted: 09 March 2022 • Accepted: 22 April 2022 • Published Online: 03 May 2022

Jijing Chen, Shuai Li, Ying Long, et al.

View Online Export Citation CrossMark

ARTICLES YOU MAY BE INTERESTED IN

A metamaterial sensor for detecting the location of a sub-wavelength object
Applied Physics Letters **120**, 181703 (2022); https://doi.org/10.1063/5.0090146

Broadband terahertz time-domain polarimetry based on air plasma filament emissions and spinning electro-optic sampling in GaP
Applied Physics Letters **120**, 181107 (2022); https://doi.org/10.1063/5.0087127

Strong interfacial coupling in vertical WSe_2/WS_2 heterostructure for high performance photodetection
Applied Physics Letters **120**, 181108 (2022); https://doi.org/10.1063/5.0082101

Webinar
Meet the Lock-in Amplifiers that measure microwaves
Oct. 6th – Register now
Zurich Instruments

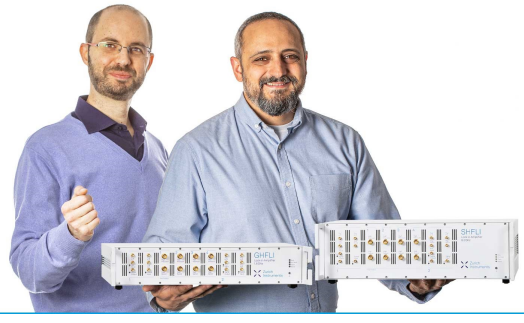

© 2022 Author(s).

Applied Physics Letters ARTICLE scitation.org/journal/apl

Nondestructive inspection of metallic microstructure chips based on photoacoustic remote sensing microscopy

Cite as: Appl. Phys. Lett. **120**, 182201 (2022); doi: 10.1063/5.0090897
Submitted: 9 March 2022 · Accepted: 22 April 2022 ·
Published Online: 3 May 2022

View Online Export Citation CrossMark

Jijing Chen,[1,2] Shuai Li,[1] Ying Long,[1,2] Xieyu Chen,[1,2] Bowen Liu,[1,3,4] Minglie Hu,[1,3,4] Jiao Li,[1,5,6,a)] and Zhen Tian[1,2,4,6,a)]

AFFILIATIONS

[1]School of Precision Instruments and Optoelectronics Engineering, Tianjin University, Tianjin 300072, China
[2]Center for Terahertz Waves, Tianjin University, Tianjin 300072, China
[3]Ultrafast Laser Laboratory, Tianjin University, Tianjin 300072, China
[4]Key Laboratory of Optoelectronics Information and Technology (Ministry of Education), Tianjin 300072, China
[5]Tianjin Key Laboratory of Biomedical Detecting Techniques and Instruments, Tianjin University, Tianjin 300072, China
[6]Georgia Tech Shenzhen Institute (GTSI), Tianjin University, Shen Zhen 518067, China

[a)]**Authors to whom correspondence should be addressed:** jiaoli@tju.edu.cn and tianzhen@tju.edu.cn

ABSTRACT

Nondestructive testing of packaged chips is essential for ensuring product performance, yet existing methods have serious drawbacks. Here, we apply photoacoustic remote sensing microscopy using a high-frequency pulse laser with a pulse width of 1.2 ps and a wavelength of 1030 nm to inspect silicon-based semiconductor chips for internal defects. Joint optical-mechanical scanning allowed high-resolution imaging of a large field of view. The basis for photoacoustic imaging was explained using a solid-state physics model, which was confirmed experimentally by measuring photoacoustic amplitudes at different doping concentrations. Our method appears capable of rapidly imaging chips over a large field of view with depth-to-resolution ratios of around 200 without the need for a couplant, which could support nondestructive inspection in industrial applications.

Published under an exclusive license by AIP Publishing. https://doi.org/10.1063/5.0090897

Flip chips with complex structures can suffer defects such as solder defects, lifted or missing leads, voids, cracks, missing soldering bumps, underfilling, and delamination,[1–3] all of which can compromise chip performance in computers, automobiles, and other electronic devices. Several nondestructive testing techniques have been proposed to detect such defects during packaging in order to ensure quality control compatible with fast production turnaround. X-ray computed tomography, for example, can reconstruct 3D defects at considerable depths, but it requires ionizing radiation, long scan time, and parallel computing.[4–6] Scanning acoustic microscopy can detect defects as deep as 200 μm, but it requires a long scan time and the chips must first be covered in an ultrasonic couplant. Surface acoustic wave techniques can also penetrate as deep as 200 μm, but it requires piezoelectric elements with limited bandwidth[7] or less sensitive air-coupled transducers together with a costly scanning laser vibrometer.[8] Ultrafast optical laser ultrasonics can detect defects to depths of several millimeters at the sub-micron resolution, but the need for motorized stage scanning limits the scanning speed.[9]

In this way, current techniques for nondestructive testing do not simultaneously combine high depth-to-resolution ratios with sensitivity, fast scanning, and freedom from ionizing radiation. An alternative may be photoacoustic microscopy, which has recently been applied to nondestructive testing.[10–13] A major limitation, however, is that photoacoustic microscopy, such as ultrasonic imaging, relies on ultrasonic transducers. This means that the gap between the transducer and the flip-chip needs to be filled with water or ultrasound gel as a couplant.[14] Couplants may damage chips, such as by corroding the metal components. The air-coupled transducer-based non-contact photoacoustic detection method has the advantage of simple configuration, while this method suffers from the low signal-to-noise ratio and the limited spatial resolution, unsuitable for nondestructive testing of chips.[15–18]

Published under an exclusive license by AIP Publishing

It may be possible to eliminate the need for couplants by integrating photoacoustic remote sensing (PARS) into a microscopic system. PARS is a non-contact measurement technique that can provide a high depth-to-resolution ratio, high sensitivity, rapid imaging, and large field of view (FOV) in biomedical applications.[19–28] The sensing is based on the elasto-optical effect: the absorber experiences photoacoustic pressure, which alters the absorber's refractive index, and this change in the index is detected by a non-interferometric detection method.[19]

In this Letter, we demonstrate the potential of PARS microscopy for nondestructive testing of metal-containing chips, and we suggest an explanation for the imaging mechanism. First, we show that PARS can detect strong contrast at the silicon–metal interface when the silicon layer is several hundred micrometers thick. We propose a solid-state physics model to explain how this contrast is imaged. We image several silicon–metal interfaces involving different types and thicknesses of silicon, and we compare the images to the corresponding brightfield micrographs. Finally, we use optical-mechanical scanning to image a FOV of $4 \times 4\ \mathrm{mm}^2$. This Letter explores another application of PARS microscopy other than bioimaging, and we wish that PARS can provide an optional idea for nondestructive testing of chips.

When using PARS for nondestructive testing, incident photons with an energy greater than the bandgap of intrinsic silicon (1.12 eV) produce both electronic and thermal stresses, which simultaneously generate opposite photoacoustic waves,[29]

$$V_{Si} = \frac{K\pi a^2}{j\omega}(1 - R_{Si})\frac{I_0}{h\nu}\Delta^0|_{r,z=0} \times \left[\frac{\alpha}{\rho C}\left(h\nu - E_g - 3k_BT\right) + \frac{1}{3}\frac{dE_g}{dP}\right], \quad (1)$$

where the first term is the thermal stress caused by optical absorption; the second term is the electronic stress caused by the photogeneration of carriers, corresponding to the pressure dependence at the semiconductor energy gap at a constant temperature; α is the linear coefficient of thermal expansion; V_{si} is the voltage of the detected photoacoustic pressure; K is the constant of proportionality; ω is the angular frequency; j is an imaginary constant; R_{si} is the optical reflectivity of the material; I_0 and $h\nu$ are light intensity and photon energy, respectively; $\Delta^0|_{r,z\,=\,0}$ is the volume expansion at the boundary; k_BT is the energy scale factor at room temperature; and E_g is the energy bandgap of the semiconductor.

Electronic stress contributes minimally to the photoacoustic pressure because of the low concentration of photogenerated carriers in intrinsic silicon, so the thermal stress dominates. In order to confirm that the PARS signal depended on the concentration of photogenerated carriers, we doped silicon chips with the increasing amount of boron or phosphorus atoms and measured the photoacoustic pressure (see the supplementary material, Fig. S1 for more details). With the increasing doping concentration, the photoacoustic signal gradually weakened and disappeared completely up to an n- or p-type doping concentration of $2.05 \times 10^{19}\ \mathrm{cm}^{-3}$. We reasoned that the thermal stress mainly contributes to the photoacoustic signal of intrinsic silicon (undoped). The electronic stress of Eq. (1) increases sharply due to the sharp increase in the number of carriers of doped silicon. Both electronic stress and thermal stress contribute to the increase in the amplitude of the photoacoustic signal. Nevertheless, the electronic stress, opposite to the thermal stress,[29] causes the thermal stress to be offset at the high doping concentration, resulting in the disappeared photoacoustic signal. Notably, the disappeared photoacoustic signal means the total stress is zero, rather than the absorption coefficient is zero in the high doping concentration. Experimental values of absorption coefficients for doped silicon[30] also support this view.

Figure 1(a) shows the experimental setup of the PARS microscope for nondestructive testing. The sample is excited using a collimated, near-infrared pulsed laser beam operating at 1030 nm with ultrashort pulses of ~1.2 ps at a high repetition frequency of 0.1–1 MHz (BFL-1030-20B from Tianjin BWT Laser Ltd., Tianjin, China). A pulsed laser delivers a collimated beam that is expanded by a pair of lenses L1 (AC1909-B from LBTEK, Shenzhen, China) and L2 (MCX10610-B from LBTEK) and that passes through a 25-μm pinhole (P25C from Thorlabs, Newton, NJ, USA) to deliver light with a diameter of about 8 mm. The beam that splits off from the beam splitter is then fed into a 350-MHz photodiode (DET10A from Thorlabs) to provide triggering. A dichroic mirror (DMSP1180 from Thorlabs) combines the excitation beam with the probe beam, which is the low-coherence 1310 nm continuous wave from superluminescent diodes (SLD1018P from Thorlabs) with the 45 nm bandwidth and the 30 mW maximum power. The interrogation beam collimated by a reflective collimator (RC08FC-P01 from Thorlabs) passes through a polarizing beam splitter (PBS254/M from Thorlabs) and a quarter-wave plate (WPQ10M-1310 from Thorlabs) to emerge as a circularly

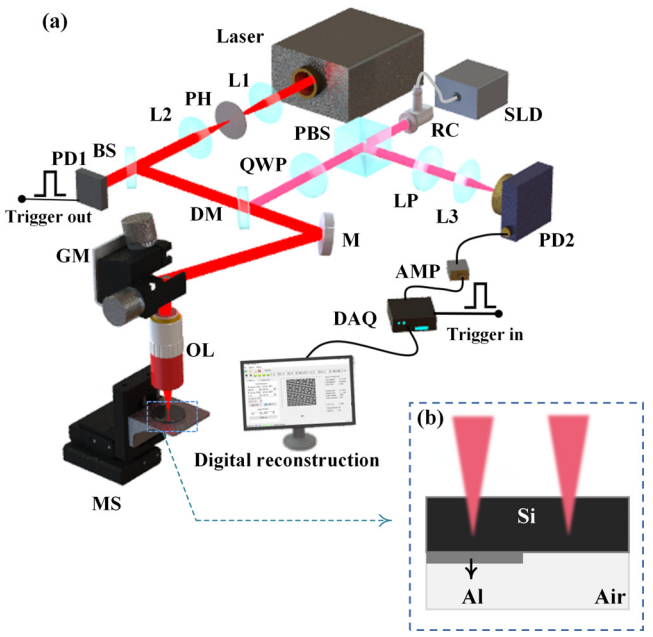

FIG. 1. PARS system for nondestructive testing and its characterization. (a) Schematic of the system, featuring a pulsed laser with a wavelength of 1030 nm, a pulse width of 1.2 ps, and a repetition frequency of 0.1–1 MHz. AMP, amplifier; BS, beam splitter; DAQ, data acquisition card; DM, dichroic mirror; GM, galvanometer; L, lens; LP, long-pass filter; M, mirror; MS, motorized stage; OL, objective lens; PBS, polarized beam splitter; PD, photodiode; PH, pinhole; QWP, quarter-wave plate; RC, reflective collimator; SLD, super-luminescent diodes. (b) Schematic of an Al–Si interface (left) and Si–air interface (right), showing the stronger elastic-optical effect for the Si–Al interface because of the stronger thermal expansion by the metal.

Published under an exclusive license by AIP Publishing

polarized light. The ultrafast pulsing of 1.2 ps is essential to satisfy the conditions for pressure relaxation and thermal relaxation given the high speed of sound and high thermal diffusivity of aluminum and silicon (see the supplementary material, Table S1 for more details). Both beams pass through the galvanometer scanning mirror system (GVS012/M from Thorlabs) and are con-focused through the objective lens (MY20X-824 from Mitutoyo, Japan). The back-reflected component of the probe beam is returned through the system and directed into the photodiode (1811-FS from New Focus, Irvine, CA, USA) after passing through a long-pass filter (FEL1250 from Thorlabs) and the best form lens (LBF254-040 from Thorlabs). The output of the photodiode is amplified using an RF amplifier (CLC-10K0.5G-5510S from Connphy Microwave Inc.) with a bandpass filter (1.8–22 MHz) and a gain of 63 dB. Then, the output is digitized using a four-channel, 14-bit PCI digitizer (CES1442 from GaGe, Lockport, IL, USA) operating at 200×10^6 samples per second. The galvanometer scanning mirror system is combined with a 3D motorized stage (M-112.2DG1 from PI, Auburn, MA, USA) to image large FOVs rapidly. The scanning speed of the motorized stages was 1.8 mm/s.

The wavelength of the near-infrared excitation light was selected to be 1030 nm to allow penetration to a depth of a few hundred micrometers given the absorption coefficient of silicon ($22\ cm^{-1}$). The excitation pulse energy was 300 nJ, with an interrogation power of around 3 mW. The FOV in a single frame was $450 \times 450\ \mu m^2$. The galvanometer was driven by a sine wave, and the scan rate was 2 Hz along the slow axis and 400 Hz along the fast axis of the galvanometer. The peak-to-peak value was extracted from A-lines and discretized, and linear interpolation was used to form the final image.

To demonstrate the performance of our PARS system, we imaged carbon fibers 7 μm in diameter sandwiched between two glass coverslips, each 100 μm thick [Fig. 2(a)]. The lateral resolution of the system was approximately 2.3 μm [Fig. 2(b)]. To evaluate the ability of our system to detect defects inside the chip, we used photolithography to prepare a 200 nm-thick aluminum pattern on a 100 μm-thick intrinsic silicon wafer (see the supplementary material, Fig. S2 for more details). Here, the aluminum film is under the silicon wafer, which is invisible to a brightfield microscope [Fig. 1(b)]. PARS microscopic imaging detected the metal-enhanced signal of silicon, which can distinguish the metal patterns at a depth of 100 μm [Fig. 2(c)]. We validated this imaging using brightfield microscopy [Fig. 2(d)].

We rationalized the PARS images in the following way. The high absorption coefficient of aluminum at 1030 nm leads to strong local heating of the metal, which generates large photoacoustic pressure. Given the high speed of sound and thermal diffusivity of aluminum and silicon, both pressure and heat diffuse from the metal layer into the silicon substrate within tens of nanoseconds. The resulting pressure at the interface of silicon is much greater than that at the interface of silicon with air, leading to a greater change in the refractive index of silicon at the metal interface.

Not only intrinsic silicon but also n- or p-doped silicon is used to produce flip chips. Therefore, we imaged samples prepared from silicon featuring n- or p-type doping. Two types of samples were identical except that the thickness was 525 μm for n-doped samples and 480 μm for p-doped samples. We performed a resolution characterization of the 525 μm sample (see the supplementary material, Fig. S4 for more details). Ultrasonic oscillations were applied during sample preparation in order to induce defects in the metallic structure, mimicking

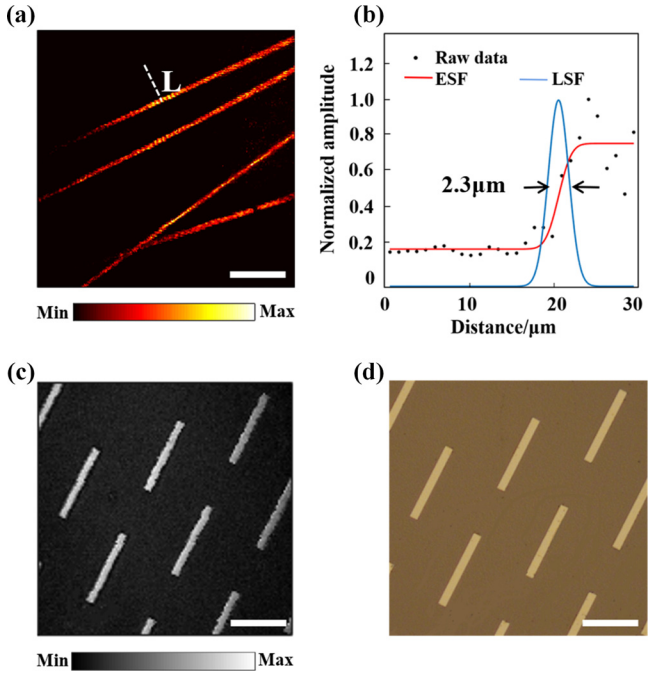

FIG. 2. Imaging results of carbon fiber and intrinsic Si–Al. (a) Optical scanning image of a network of carbon fibers with a diameter of 7 μm. (b) The line spread function (LSF) and edge spread function (ESF) from the data in panel (a). The ESF was extracted directly from the voltage signal of single carbon fiber, and the LSF was calculated from the ESF. The full-width-at-half-maximum (FWHM) lateral resolution was estimated as 2.3 μm. (c) PARS imaging of an aluminum strip of 200 nm thick that had been vapor-deposited onto intrinsic Si that was 100 μm thick. (d) Brightfield micrograph of the same sample as in panel (c). Scale bar: 100 μm. The brightfield micrograph was taken from the Al side (see supplementary material, Fig. S3 for more details).

internal defects such as cracks and voids. The PARS microscopy system easily detected the defects, while also demonstrating good imaging depth (Fig. 3).

Next, we asked whether the PARS microscopy system could scan large FOVs at high resolution. To this end, we combined mechanical and optical scanning. In this approach, a large FOV was built up as a "mosaic" of many smaller FOVs: a small FOV was scanned by the galvanometer, then the motorized stages, working in the discrete movement mode, moved to the adjoining small FOV, which overlapped with the first by about $20 \times 450\ \mu m^2$. In this way, we stitched together mosaics of 10×10 smaller FOVs of $450 \times 450\ \mu m^2$ into one large FOV of $4 \times 4\ mm^2$, suitable for industrial nondestructive testing. We applied this "mosaic acquisition" to a silicon wafer 525 μm thick with n-type doping. The repetition frequency was 200 kHz, scanning took about 50 s, and data were streamed to ensure that data transfer was not limiting. PARS microscopy provided a clear metal image and located defects over a large FOV (Fig. 4). We found that during scanning, beam incidence is uneven over the objective lens and depends on the scanning angle, creating slight inhomogeneity in each frame. As a result, the range per frame is limited to 450 μm.

Our PARS microscopy system appears to be another use of PARS for imaging silicon–metal interfaces and could be an opportunity for nondestructive testing of chips. We demonstrate here the ability to

Published under an exclusive license by AIP Publishing

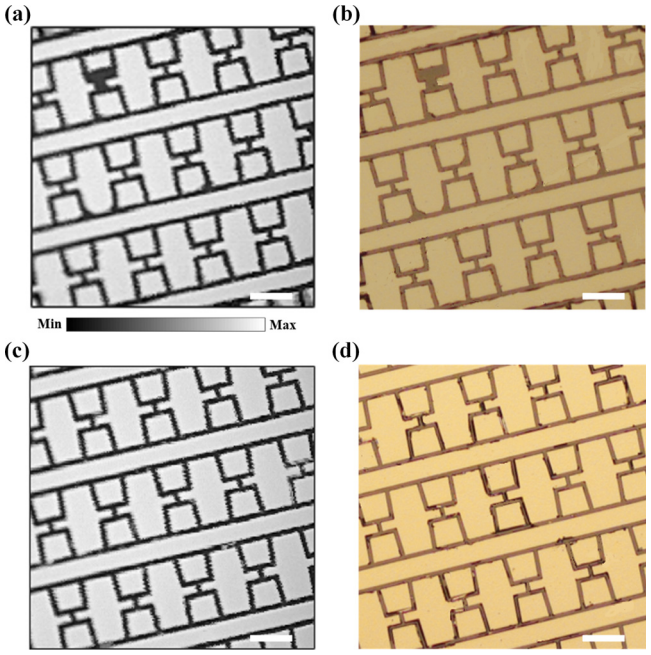

FIG. 3. Ability of PARS microscopy to nondestructively detect defects in doped silicon chips. Doped samples were prepared, then subjected to ultrasonic oscillations at an ultrasonic power level of 80%. (a) Imaging of a silicon–metal sample at an n-type doping concentration of 2.34×10^{15} cm^{-3}. The image was taken from the silicon face. (b) The corresponding brightfield image of the sample in panel (a) was taken from the metal face. (c) Imaging of a silicon-metal sample at a p-type doping concentration of 1.64×10^{18} cm^{-3}. The image was taken from the silicon face. (d) The corresponding brightfield image of the sample in panel (c) was taken from the metal face. Scale bar: 100 μm. The brightfield micrographs were taken from the Al side.

rapidly scan a large FOV at a high depth-to-resolution ratio of around ~200 (see supplementary material, Fig. S4 for more details), and we validate the system on industry-realistic silicon samples with n- or p-type doping. Based on solid-state physics principles and our experiments, we propose a simple model to explain how the silicon-metal systems are imaged; this model differs from that for the photoacoustic imaging of biological materials.[19]

While the PARS microscopy system described here already shows substantial potential for integration into industrial pipelines, we can easily imagine numerous improvements in the future. Using an excitation laser with repetition frequencies in the MHz range may accelerate scanning, and using a tube lens may solve the problem of uneven illumination and expand FOV during optical scanning. It may be possible to integrate machine learning or other approaches into this system to support real-time image processing, which may lead to fully automated nondestructive testing. Further work should verify and extend our results by taking into account the decay length of photons in silicon materials, the lifetime of photogenerated carriers, and more complex mechanisms of carrier recombination. More generally, future studies should explore in more detail how to image non-biological solid materials based on the photoacoustic and elasto-optical effects.

In conclusion, we describe the PARS system involving ultrashort pulses of near-infrared excitation light at 1030 nm that can clearly

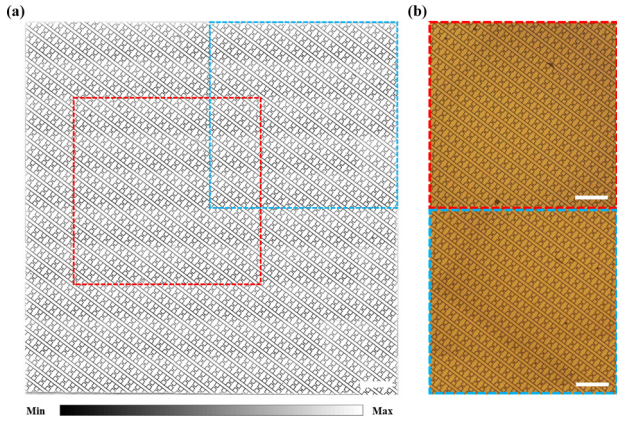

FIG. 4. Combining a 3D mechanical stage with optical scanning to nondestructively image a large FOV of 4×4 mm^2 using PARS microscopy. The sample was a silicon-metal sample 525 μm thick and n-doped at a concentration of 2.34×10^{15} cm^{-3}. (a) PARS micrograph. (b) Corresponding brightfield micrograph. Scale bar: 300 μm. The brightfield micrographs were taken from the Al side.

image the metal structure beneath different types of Si materials up to 525 μm thick. We verified that PARS can deliver high spatial resolution, high speed, and high depth-to-resolution ratio. In addition, the combination of mechanical and optical scanning in PARS allows imaging of large FOVs. These results suggest the potential of PARS for nondestructive testing of chips in industrial settings.

See the supplementary material that describes the experimental verification for the model and the computation results of pressure relaxation conditions and thermal relaxation conditions. Detailed sample preparation processes and corresponding resolution characterization are also included. Additional experimental details in this Letter are also explained.

This work was supported by the National Natural Science Foundation of China (No. 82171989), the National Key Research and Development Program of China (No. 2017YFA0701004), Tianjin Municipal Fund for Distinguished Young Scholars (Grant No. 20JCJQJC00190), Key Fund of Shenzhen Natural Science Foundation (Grant No. JCYJ20200109150212515).

AUTHOR DECLARATIONS

Conflict of Interest

The authors have no conflicts to disclose.

Author Contributions

J.C. and S.L. contributed equally to this work.

DATA AVAILABILITY

The data that support the findings of this study are available from the corresponding authors upon reasonable request.

REFERENCES

[1]G. W. A. Dummer and P. Chakravarthi, IEEE Aerosp. Syst. Mag. **13**, 39 (1998).

Published under an exclusive license by AIP Publishing

[2]M. Holler, M. Guizar-Sicairos, E. Tsai, R. Dinapoli, E. Müller, O. Bunk, J. Raabe, and G. Aeppli, Nature **543**(7645), 402–406 (2017).
[3]S. Brand, P. Czurratis, and P. Hoffrogge, Microelectron. Reliab. **50**(9–11), 1469–1473 (2010).
[4]J. C. E. Mertens, J. J. Williams, and N. Chawla, J. Electron. Mater. **43**(12), 4442–4456 (2014).
[5]A. Teramoto, T. Murakoshi, M. Tsuzaka, and H. Fujita, IEEE Trans. Electron. Packag. Manuf. **30**(4), 285–292 (2007).
[6]M. Holler, M. Odstrcil, M. Guizar-Sicairos, M. Lebugle, E. Müller, S. Finizio, G. Tinti, C. David, J. Zusman, W. Unglaub, O. Bunk, J. Raabe, A. Levi, and G. Aeppli, Nat. Electron. **2**(10), 464–470 (2019).
[7]P. Aryan, A. Kotousov, C. T. Ng, and S. Wildy, Smart Mater. Struct. **25**(3), 035018 (2016).
[8]T. Y. Sunarsa, P. Aryan, I. Jeon, B. Park, P. Liu, and H. Sohn, Materials **10**(12), 1402 (2017).
[9]Y. Gao, H. Lee, and J. Jiao, Opt. Express **26**(25), 32812–32823 (2018).
[10]L. Wang and J. Yao, Nat. Methods **13**(8), 627–638 (2016).
[11]S. Jeon, J. Kim, J. P. Yun, and C. Kim, J. Opt. **18**(11), 114001 (2016).
[12]K. Nakahata, K. Karakawa, K. Ogi, K. Mizukami, K. Ohira, M. Maruyama, S. Wada, T. Namita, and T. Shiina, Ultrasonics **98**, 82–87 (2019).
[13]H. Liu, Y. Zhao, J. Zhou, P. Li, S. Bo, and S. Chen, ACS Appl. Energy Mater. **3**(2), 1260–1264 (2020).
[14]S. Chen and C. Tian, Vis. Comput. Ind. Biomed. Art **4**(1), 6 (2021).
[15]X. L. Dean-Ben, G. A. Pang, F. M. Espinosa, D. Razansky *et al.*, Appl. Phys. Lett. **107**(5), 051105 (2015).
[16]G. J. Tserevelakis, P. Siozos, A. Paoanikolaou, K. Melessanaki, G. Zacharakis *et al.*, Ultrasonics **98**, 94 (2019).
[17]H. G. Ma, K. D. Xiong, J. W. Wu, X. R. Ji, S. H. Yang *et al.*, Appl. Phys. Lett. **114**(13), 133701 (2019).
[18]C. Ozsoy, J. N. Xu, J. Li, F. M. Espinosa, D. Razansky, X. Luis *et al.*, AIP Adv. **12**(3), 035043 (2022).
[19]P. Hajireza, W. Shi, K. Bell, R. J. Paproski, and R. J. Zemp, Light. Sci. Appl. **6**, e16278 (2017).
[20]P. H. Reza, K. Bell, W. Shi, J. Shapiro, and R. J. Zemp, Optica **5**(7), 814–820 (2018).
[21]K. L. Bell, P. H. Reza, and R. J. Zemp, Opt. Lett. **44**(14), 3466–3469 (2019).
[22]B. R. Ecclestone, K. Bell, S. Abbasi, D. Dinakaran, M. Taher, J. R. Mackey, and P. H. Reza, Biomed. Opt. Express **12**(1), 654–665 (2021).
[23]S. Abbasi, D. Dinakaran, G. Bigras, J. R. Mackey, and P. H. Reza, Opt. Lett. **45**(17), 4770–4773 (2020).
[24]N. J. M. Haven, P. Kedarisetti, B. S. Restall, and R. J. Zemp, Opt. Lett. **45**(2), 535–538 (2020).
[25]S. Abbasi, M. Le, B. Sonier, K. Bell, D. Dinakaran, G. Bigras, J. R. Mackey, and P. H. Reza, Biomed. Opt. Express **10**(11), 5461–5469 (2019).
[26]P. Kedarisetti, N. J. M. Haven, B. S. Restall, M. T. Martell, and R. J. Zemp, Opt. Lett. **45**(16), 4559–4562 (2020).
[27]K. Bell and P. H. Reza, Opt. Lett. **45**(13), 3427–3430 (2020).
[28]J. Zhou, W. Wang, L. Jing, and S. Chen, Opt. Lett. **46**(5), 997–1000 (2021).
[29]R. G. Stearns and G. S. Kino, Appl. Phys. Lett. **47**(10), 1048–1050 (1985).
[30]S. E. Aw, H. S. Tan, and C. K. Ong, J. Phys.: Condens. Matter **3**(2), 8213 (1991).

Published under an exclusive license by AIP Publishing